



Contents lists available at SciVerse ScienceDirect

International Journal of Heat and Mass Transfer

journal homepage: www.elsevier.com/locate/ijhmt

Heat transfer and pressure drop characteristics of peripheral-finned tube heat exchangers

Bruno F. Pussoli^a, Jader R. Barbosa Jr.^{a,*}, Luciana W. da Silva^b, Massoud Kaviany^c^a Polo – Research Laboratories for Emerging Technologies in Cooling and Thermophysics, Department of Mechanical Engineering, Federal University of Santa Catarina, Florianopolis, SC 88040-900, Brazil^b Embraco Compressors, Joinville, SC 89219-901, Brazil^c Department of Mechanical Engineering, University of Michigan, Ann Arbor, MI 48109-2125, USA

ARTICLE INFO

Article history:

Received 11 May 2011

Received in revised form 16 January 2012

Accepted 16 January 2012

Keywords:

Heat exchanger

Enhanced heat transfer

Peripheral fin

Porous media

ABSTRACT

The peripheral-finned tube is a new geometry aimed at avoiding moisture-condensate blockage hindering of the air-side heat transfer, by allowing for robust air flow pathways. It consists of a porous structure formed by periodic, radial-hexagonal fin arrangements of different radial extents mounted with a 30° offset from its neighboring level. Here, the air-side pressure drop and the heat transfer characteristics of five different heat exchanger prototypes with different geometric characteristics, such as the radial fin length, fin distribution, and heat exchanger length, were evaluated experimentally in an open-loop wind-tunnel calorimeter. The results demonstrate the effective performance, i.e., the pressure drop and heat transfer characteristics, of this new heat exchanger. A one-dimensional theoretical model based on the porous media treatment was also developed to predict the thermal-hydraulic behavior of the heat exchanger. The model incorporates the actual fin geometry into the calculation of the air-side porosity. The air-side permeability is calculated according to the Kozeny–Carman model and the particle-diameter based analysis. The model predicts the experimental data within a few percent RMS, depending on the correlations used for the friction coefficient and interstitial Nusselt number.

© 2012 Elsevier Ltd. All rights reserved.

1. Introduction

Compact heat exchangers are commonly used in applications involving gases, since the large external surface area per unit volume compensates the low heat transfer coefficients associated with the air flow. A large area density on the air side is usually obtained by means of extended surfaces (fins). The heat transfer fundamentals and the state of the art in the thermal design of enhanced surfaces have been reviewed recently by Shah and Sekulic [1] and Webb and Kim [2]. Tube-fin heat exchangers, in particular, are largely used as evaporators in refrigeration systems due to their relatively low cost, simple manufacture methods and availability of well-established correlations for thermal-hydraulic (heat transfer and pressure drop) design. A number of different extended surface geometries have been proposed to this date with the primary aim of reducing the tube-fin heat exchanger volume by increasing the air-side thermal conductance to a level compatible with specific pressure drop and/or pumping power constraints [2]. Wang [3,4] presented a review of patents issued on enhanced surfaces for fin-and-tube heat exchangers. Jacobi et al. [5] reviewed

the existing correlations for heat transfer and pressure drop in round and flat tube-fin heat exchangers.

In the presence of latent heat transfer from the moist air to the heat exchanger surface, the condensate, ice or frost accumulated on the fins and tubes need to be removed periodically to avoid the partial or complete blockage of the air flow channels. This obstruction deteriorates the thermal performance of the evaporator. When frost is formed on the surface, the performance decline is due to (i) an increase of the conduction thermal resistance due to the relatively low thermal conductivity of the frost layer and (ii) a reduction of the air flow rate due to the increased air-side pressure drop. Recent reports demonstrate that the increase in the friction factor and the decrease in the heat transfer rate in wetted finned coils can be as high as 70% and 100%, respectively [6,7]. For removal of condensate from the fin surface, electrowetting has been suggested [8,9]. For conditions typical of evaporators encountered in household refrigerators, Knabben et al. [10,11] demonstrated that the air-side pressure drop can increase by 100% or more over the course of time of a typical defrost cycle. This can reduce the air volume flow rate and the heat transfer rate to the coil by as much as 50%.

From a thermodynamic perspective, some defrosting methods currently used are particularly inefficient and fundamentally irreversible. Electric heaters are utilized in household and light

* Corresponding author. Tel.: +55 48 32345691; fax: +55 48 32345166.

E-mail address: jrb@polo.ufsc.br (J.R. Barbosa Jr.).

Nomenclature

A	area [m ²]
A_c	cross-section area [m ²]
c_p	specific heat capacity at constant pressure [J/kg K]
D	diameter [m]
D_p	particle diameter [m]
f	friction factor [-]
\bar{h}	average heat transfer coefficient [W/m ² K]
k	thermal conductivity [W/m K]
K_c	contraction coefficient [-]
K_e	expansion coefficient [-]
L	length [m]
\dot{m}	mass flow rate [kg/s]
n	number of data points [-]
N_k	number of fins of the k th arrangement [-]
Nu	Nusselt number [-]
p	pressure [Pa]
P	perimeter [m]
\dot{Q}	heat transfer rate [W]
Re	Reynolds number [-]
T	temperature [K]
U_f	face velocity [m/s]
UA	overall thermal conductance [W/K]
\dot{V}	volume flow rate [m ³ /s]
x	distance [m]

Greek symbols

β	surface area per unit volume [m ² /m ³]
ΔT_{LM}	log-mean temperature difference [K]

ε	porosity [-]
η_k	fin efficiency of the k th fin arrangement [-]
η_o	overall surface efficiency [-]
ρ	density [kg/m ³]
ν	kinematic viscosity [m ² /s]
θ	excess temperature ($=T_s - T$) [K]

Subscripts

a	air
b	fin base
$bare$	bare tube
ctc	contact
CV	control volume
i	internal
in	inlet
o	external
out	outlet
p	peripheral fin
r	radial fin
s	solid wall
tip	fin tip
w	water

Abbreviations

AAD	absolute average deviation
RMS	root mean square

commercial systems to eliminate the frost build-up on the heat exchanger surface. During normal operation, the heater is periodically switched on in order to melt the frost accumulated on the evaporator. Thus, not only high grade energy (in the form of electricity) is dissipated as heat in the melting process, but this irreversible energy conversion takes place inside the freezer compartment, which represents an extra thermal load on the refrigeration system. Typical values of the defrost efficiency, defined as the ratio of the amount of energy required to melt the frost and the actual electrical energy dissipated as heat during the defrost mode, are of the order of 5–15%. Therefore, new approaches are needed –both in terms of defrost strategy and frost-robustness of the components – in order to minimize the thermodynamic performance penalty associated with the frost management in household and light commercial refrigeration appliances.

Recently, Wu et al. [12] proposed a novel air-side heat exchanger geometry for enhanced heat transfer performance under dehumidifying conditions. The *peripheral finned-tube evaporator* (see Fig. 1) is a cross-flow heat exchanger whose air-side is composed by a hexagonal arrangement of open-pore cells formed by radial fins whose bases are attached to the tubes and whose tips are connected to the peripheral fins. Each fin arrangement is constructed with six radial fins and six peripheral fins forming a hexagon-like structure. The air-side fin configuration is composed of three levels of fin arrangement, each characterized by the length of radial fin and mounted with a 30° offset from its neighbouring level. Wu et al. [12] advanced a mathematical model for the heat transfer in the radial and peripheral fins and carried out preliminary computational fluid dynamics (CFD) simulations to investigate the air flow distribution with and without frost build-up in the vicinity of the tubes. Since heat conduction in the radial fins is an important mechanism of heat transfer, it was claimed that frost blockage surrounding the tube would not deteriorate the thermal-hydraulic performance significantly.

In a previous paper [13], a preliminary experimental analysis of a single peripheral finned-tube evaporator prototype was conducted. In the present paper, for the first time, a systematic experimental evaluation of the thermal-hydraulic performance of the peripheral finned-tube heat exchanger is carried out. Five prototypes with different values of radial fin length, fin thickness, heat exchanger flow length, face area, and fin distribution were

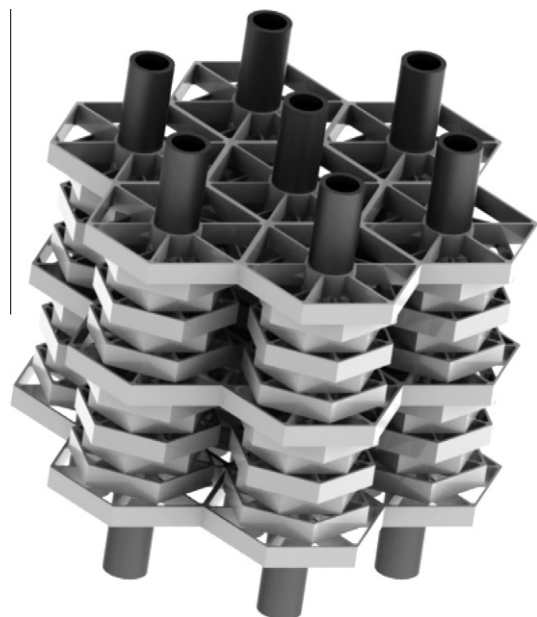


Fig. 1. The peripheral finned-tube geometry [12].

designed and constructed. The heat exchangers were tested in an open-loop wind tunnel calorimeter for air flow rates ranging from 30 to 110 m³/h, thus corresponding to face (superficial) velocities between 0.84 and 4.11 m/s. The air-side heat transfer and pressure drop data were then predicted by a 1-D mathematical model based on the theory of porous media that accounts for the conduction heat transfer in the fins and for the actual fin geometry in the calculation of the air-side porosity. The air-side permeability is calculated according to the Kozeny–Carman model with the particle diameter definition due to Whitaker. The performances of the correlations of Whitaker [14] and Handley and Heggs [15] for the particle (interstitial) Nusselt number and of Ergun [16] and Montillet et al. [17] for the friction factor were evaluated based on their prediction of the heat transfer rate and pressure drop data. As far as the pressure drop is concerned, the best overall performance of the model was obtained with the Montillet et al. [17] friction correlation, which showed an RMS error of around 3%. The performances of the Handley and Heggs [15] and of the Whitaker [14] correlations for the interstitial Nusselt number were very similar, giving RMS errors of around 1%.

2. Experimental work

2.1. Heat exchanger prototypes

Five heat exchangers were constructed from copper (tubes) and aluminum (fins). The inner and outer diameters of the tubes in all prototypes were 7.8 and 8.8 mm, respectively. After mounting the fins on the tube bank, hydraulic expansion of the tubes was performed to minimize the contact thermal resistance between the fins and tubes. A staggered tube array was used, and all samples are in a mixed-mixed cross-parallel flow configuration (see Fig. 2 for a schematic view of samples A, C, D and E). The basic dimensions of the heat exchanger samples and of the fins are shown in Table 1 (see also Fig. 3).

The fin structure is composed of three distinct levels of fin arrangement (R_1 , R_2 and R_3), each characterized by the length of the radial fin extending from the tube. All radial and peripheral fins are rectangular in cross section. A fin width of 4 mm was used in all heat exchangers. The fins were assembled with a 30° offset from their neighbors, according to the distribution shown in Table 1 for each heat exchanger. Each group of six fins comprises a so-called 'unit', as illustrated in Fig. 4.

In order to observe the influence of the fin and heat exchanger geometric parameters, the samples were constructed with similar characteristics between them. Samples A, B and C have the same heat exchanger volume (face area and length were kept fixed), but present different fin characteristics. Samples B and D have exactly the same surface area, but have different heat exchanger length and volume. Samples D and E have the same face area, but the fin arrangements are smaller than those in the other heat exchanger samples.

2.2. Experimental facility

The open-loop wind tunnel facility for the heat transfer and pressure drop measurements (Fig. 5) has been described in detail in previous work [18] and, for completeness, only its main features will be reported here. The facility was constructed from a double layer of steel plates between which a 100 mm thick layer of glass wool was inserted to provide thermal insulation. The air flow was supplied by a 51-W variable speed fan and was determined via the measured pressure drop in a bank of calibrated nozzles, according to the procedure recommended by ANSI/ASHRAE 51 [19]. The nozzle pressure drop was measured by a differential

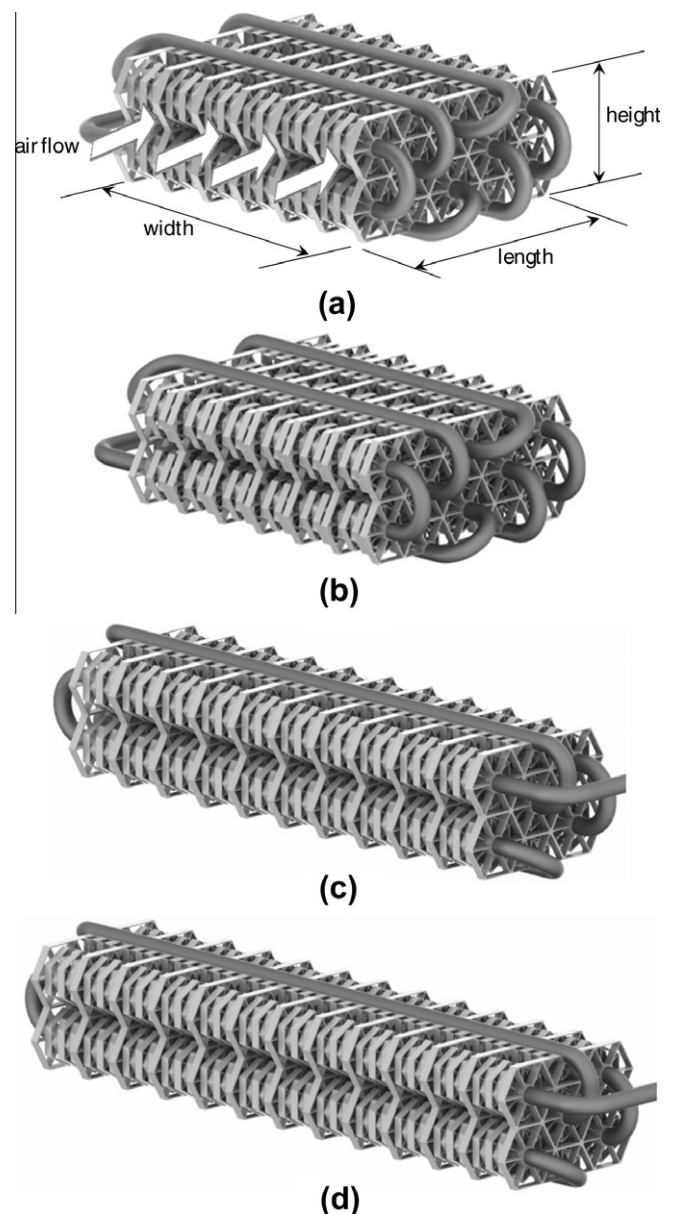


Fig. 2. Schematic view of the heat exchanger samples. (a) Sample A. (b) Sample C. (c) Sample D. (d) Sample E.

pressure transducer with a manufacturer calibration uncertainty of $\pm 0.5\%$ of the full-scale (995 Pa). Wire meshes were employed to make the flow uniform at the inlet and exit sections and also upstream of the air flow nozzles. The air temperature was measured upstream of the heat exchanger by three thermocouples, and downstream of it by six thermocouples. The thermocouples were embedded into small copper blocks (diameter and height of 10 mm) to minimize temperature oscillations during measurements. The temperature fluctuation of the ambient air entering the calorimeter was controlled to ± 0.1 °C before entering the wind tunnel [18]. The uncertainty of the temperature measurements inside the wind tunnel was ± 0.2 °C. The air-side static pressure drop was measured by mounting perforated hoses (the spacing between adjacent holes was 25 mm) on two grooves cut into bottom wall of the test section (one groove was located upstream and the other downstream of the evaporator). The grooves were perpendicular to the main flow direction and their depth was such that the pressure taps were at the same level as the bottom wall. The adjoining

Table 1
Geometric characteristics of the heat exchangers.

Sample	HX length (mm)/ no. tube rows	HX width (mm)/ no. units per tube	HX height (mm)	R ₃ Radial length (mm)/no. of fins	R ₂ Radial length (mm)/no. of fins	R ₁ Radial length (mm)/no. of fins	Fin thickness (mm)	Surface area (m ²)/β (m ² /m ³)	Porosity	Distribution
A	128.6/5	148/6	56	12.1/70	9.0/180	7.0/120	0.5	0.4043/381	0.877	R ₃ , R ₂ , R ₁ , R ₂ , R ₁ , R ₂
B	128.6/5	148/6	56	12.1/70	9.0/180	7.0/120	0.8	0.4083/385	0.810	R ₃ , R ₂ , R ₁ , R ₂ , R ₁ , R ₂
C	128.6/5	148/6	56	12.1/70	9.0/120	7.0/180	0.8	0.3945/372	0.815	R ₃ , R ₁ , R ₂ , R ₁ , R ₂ , R ₁
D	80.3/3	244/10	56	12.1/66	9.0/180	7.0/120	0.8	0.4083/372	0.810	R ₃ , R ₂ , R ₁ , R ₂ , R ₁ , R ₂
E	67.3/3	292/12	47	9.5/78	7.0/216	5.5/144	0.8	0.3939/426	0.766	R ₃ , R ₂ , R ₁ , R ₂ , R ₁ , R ₂

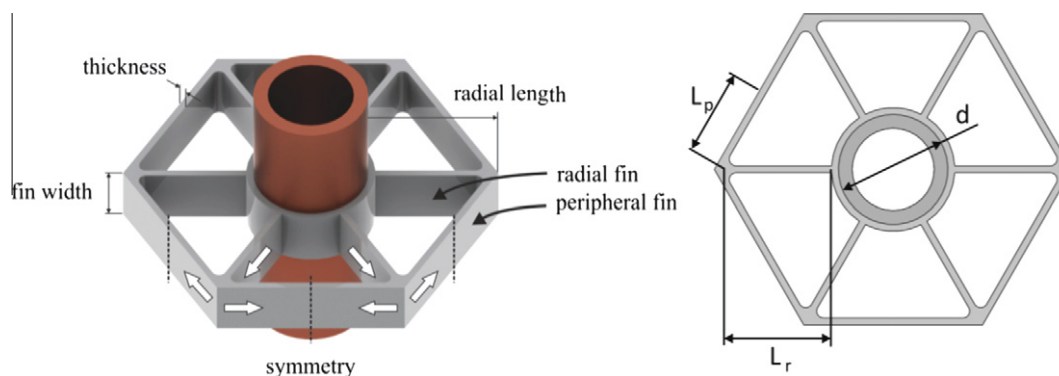


Fig. 3. Fin geometric parameters.

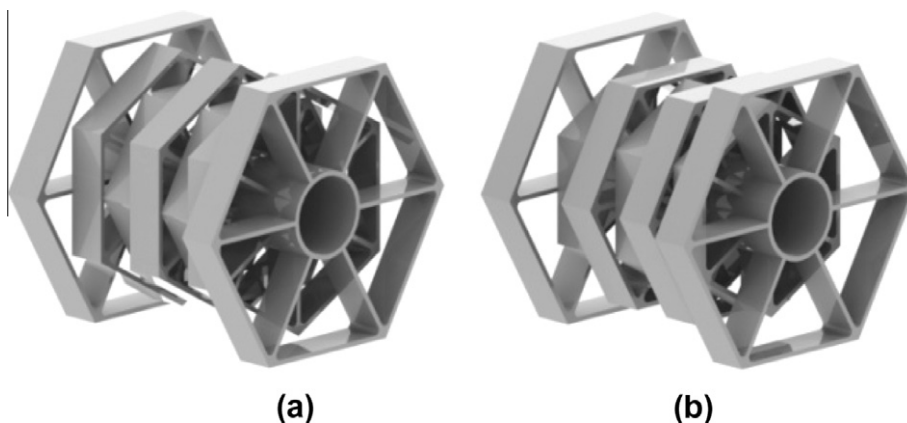


Fig. 4. Representation of a unit and its distribution. From left to right: (a) R₃, R₂, R₁, R₂, R₁, R₂, R₃ and (b) R₃, R₁, R₂, R₁, R₂, R₁, R₃.

surfaces were leveled with silicone glue to avoid disturbing the flow in the vicinity of the pressure taps. One end of each hose was connected to the differential pressure transducer while the other end was sealed. The manufacturer calibration uncertainty of the pressure transducer was $\pm 0.5\%$ of the full scale (500 Pa). A speed-controlled rotary pump, with a maximum flow rate of 4 L/min, drove the water flow inside the tubes. The flow rate was measured with a turbine flow meter with an operating range of 0.4–3.5 L/min and an *in-situ* calibration uncertainty of ± 4.5 mL/min. The water inlet temperature was set by a temperature-controlled bath with an accuracy of ± 0.1 °C. The water loop was thermally insulated and T-type immersion thermocouples (± 0.2 °C) were placed immediately upstream and downstream of the heat exchanger.

2.3. Experimental procedure

After mounting the heat exchanger into the test section, the apparatus was switched on. The tube bends were thermally insulated on both sides of the heat exchanger to prevent heat transfer to the air. The inlet water temperature was set to 40 °C in the thermostatic bath, and a few minutes were required for it to stabilize. The desired air flow rate was adjusted and the water flow rate was set in order to provide a temperature range (difference between the inlet and outlet temperatures) of 4 °C. Depending on the air flow rate, between 50 to 80 min were needed to reach steady-state. The room temperature was 20 ± 1.0 °C. The steady-state criterion has been established so that each variable was averaged over a 30-minute interval. If the absolute value of the difference between

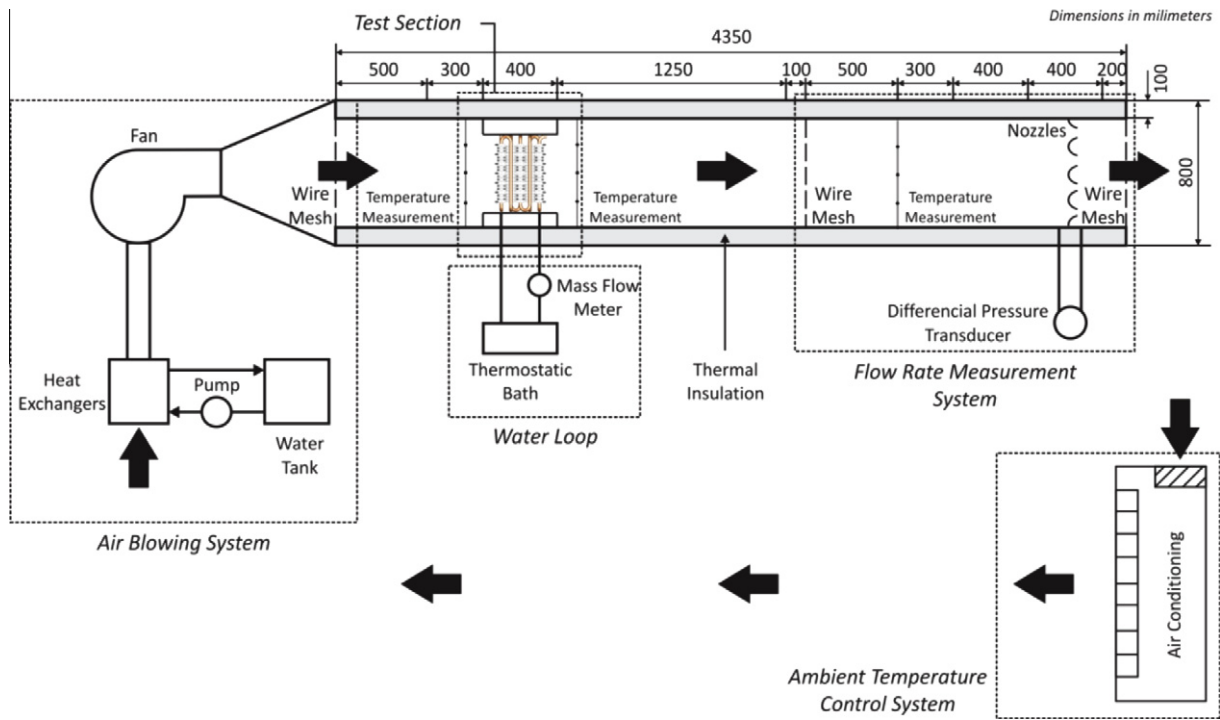


Fig. 5. The experimental facility.

the reading at the beginning of the sampling interval ($t = 0$) and at the end ($t = 30$ min) was less than three times the standard deviation of the signal in that interval, the test was steady. A test was considered valid if, in addition to being steady, the heat transfer rates calculated based on energy balances on the water side and on the air side were within $\pm 5\%$ of each other.

2.4. Data regression

The experimental air-side thermal conductance is given by,

$$\frac{1}{\eta_o \bar{h}_o A_o} = \frac{\Delta T_{LM}}{\dot{Q}} - \frac{1}{h_i A_i} \quad (1)$$

where the experimental heat transfer rate and log-mean temperature difference for parallel flow are calculated from,

$$\dot{Q} = \frac{1}{2} [\dot{m}_w c_{pw} (T_{w,in} - T_{w,out}) + \dot{m}_a c_{pa} (T_{a,out} - T_{a,in})] \quad (2)$$

$$\Delta T_{LM} = \frac{(T_{w,out} - T_{a,out}) - (T_{w,in} - T_{a,in})}{\ln \left[\frac{(T_{w,out} - T_{a,out})}{(T_{w,in} - T_{a,in})} \right]} \quad (3)$$

The water-side (internal flow) heat transfer coefficient was calculated according to the Gnielinski correlation [1].

A detailed uncertainty propagation analysis was conducted [20]. The experimental uncertainties for the volume flow rate, pressure drop, air-side thermal conductance and heat transfer rate, were estimated at $\pm 1 \text{ m}^3/\text{h}$ (maximum), $\pm 3 \text{ Pa}$, $\pm 2.5 \text{ W/K}$ and $\pm 18 \text{ W}$, respectively.

3. Modeling

The heat exchanger modeling was carried out at two distinct levels. At the fin level (first level), a calculation framework for the fin temperature profile was proposed based on the work of Wu et al. [12]. The heat exchanger (second) level consisted of 1-D energy and momentum balances to determine the air tempera-

ture and static pressure profiles along the heat exchanger. The fin temperature distribution calculated in the first level was used to determine the overall surface efficiency in the second level. Closure relationships for the air-side Nusselt number and friction factor are needed in both levels. The models were implemented on the Engineering Equation Solver (EES) platform [21].

3.1. Fin heat transfer

At the junction between each radial fin and two peripheral fins (see Fig. 3), the following heat balance holds,

$$\dot{Q}_{r,tip} = 2\dot{Q}_{p,b} \quad (4)$$

Eq. (4) is solved for the excess temperature of the radial fin tip, θ_{tip} . The excess temperature is defined as the difference between the solid local temperature and the bulk temperature of the fluid. By assuming symmetry with respect to the mid-plane of the peripheral fin, one has,

$$\dot{Q}_{p,b} = \theta_{tip} (P_p k_s A_{c,p} \bar{h}_o)^{1/2} \tanh \left[\left(\frac{P_p \bar{h}_o}{k_s A_{c,p}} \right)^{1/2} L_p \right] \quad (5)$$

By assuming prescribed excess temperatures at the base of the radial fin and at the radial fin tip, one has [12,13],

$$\dot{Q}_{r,tip} = -k_s A_{c,r} \theta_b \frac{\left((\theta_{tip}/\theta_b) \left(\frac{P_r \bar{h}_o}{k_s A_{c,r}} \right)^{1/2} \cosh \left[\left(\frac{P_r \bar{h}_o}{k_s A_{c,r}} \right)^{1/2} L_r \right] - \left(\frac{P_r \bar{h}_o}{k_s A_{c,r}} \right)^{1/2} \right)}{\sinh \left[\left(\frac{P_r \bar{h}_o}{k_s A_{c,r}} \right)^{1/2} L_r \right]} \quad (6)$$

3.2. Heat exchanger model

3.2.1. Heat transfer

The heat exchanger was divided into one-dimensional control volumes of length L_{CV} in the direction of the flow (see Fig. 6). The

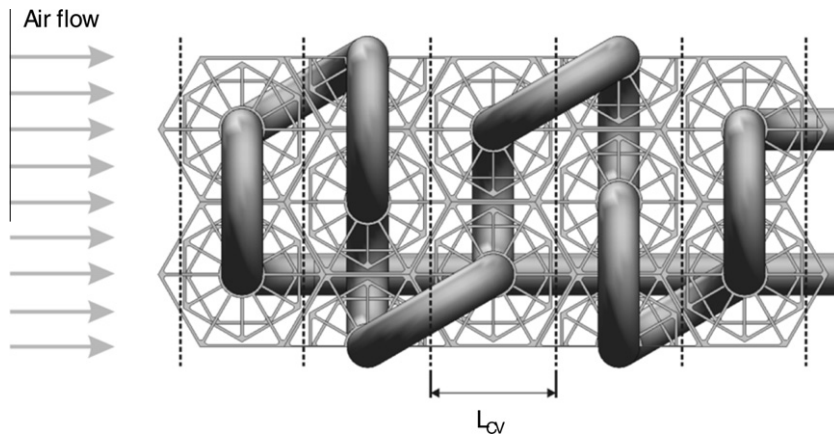


Fig. 6. Peripheral fin heat exchanger divided into control volumes.

face velocity, the face area, the inlet pressure and the inlet temperature were known. An energy balance was also carried out on the water side for each control volume. The tube wall temperature, which was assumed constant in each control volume for the sake of the fin efficiency calculation, was calculated from the average (log-mean) bulk water temperature in the control volume taking into account the (small) thermal resistance of the solid wall. The implicit form of the energy balance for each control volume is given by,

$$T_{a,out} - T_{a,in} = \frac{UA}{\dot{m}_a c_{pa}} \Delta T_{LM} \quad (7)$$

where the log-mean temperature difference in the control volume was calculated using Eq. (3). The overall heat conductance of the control volume was calculated by (the tube wall thermal resistance has been neglected),

$$\frac{1}{UA} = \frac{1}{\eta_o \bar{h}_o A_o} + \frac{1}{\bar{h}_i A_i} \quad (8)$$

where, again, the internal (water-side) heat transfer coefficient was calculated from the Gnielinski correlation. It should be mentioned that the air-side heat transfer surface in the control volume, A_o , was known exactly for each heat exchanger prototype. The overall surface efficiency was calculated analytically for each control volume based on the following relationship,

$$\eta_o = \frac{\eta_1 N_1 A_1 + \eta_2 N_2 A_2 + \eta_3 (N_3 A_3 - A_{ctc})}{N_1 A_1 + N_2 A_2 + (N_3 A_3 - A_{ctc})} \quad (9)$$

where η_k , N_k and A_k ($k = 1, 2, 3$) are the fin efficiency, number of fins and fin surface area for each arrangement. A_{ctc} is the contact area of the R_3 fins touching each other between adjacent control volumes. The fin efficiency of a fin arrangement is given by,

$$\eta_k = \frac{6\dot{Q}_{r,b} + \bar{h}_o A_{bare} (T_s - T_a)}{\bar{h}_o A_o (T_s - T_a)} \quad (10)$$

where A_{bare} is the area around the periphery of the tube that is in direct contact with the air. The heat transfer rate at the base of the radial fin was calculated from Fourier's law as follows,

$$\dot{Q}_{r,b} = -k_s A_{c,r} \left. \frac{d\theta_r}{dx} \right|_{x=0} \quad (11)$$

where x is the distance from the base of the radial fin.

The heat transfer coefficient between the air and the solid surfaces has been defined according to the heat transfer theory for discontinuous solid surfaces and large specific surface areas [22],

$$\bar{h}_o = k_a \frac{Nu_{D_p} (1 - \varepsilon)}{D_p \varepsilon} \quad (12)$$

where ε is the heat exchanger porosity (i.e., the volume fraction occupied by the air) and D_p is the equivalent particle diameter defined as six times the ratio of the solid volume and the air-side heat transfer surface area. In the present paper, the Nusselt number was estimated via the correlations due to Whitaker [14],

$$Nu_{D_p} = 2 + \left(0.4 Re_{D_p}^{1/2} + 0.2 Re_{D_p}^{2/3} \right) Pr_a^{0.4} \quad (13)$$

and due to Handley and Heggs [15],

$$Nu_{D_p} = \frac{0.255}{\varepsilon} Pr_a^{1/3} Re_{D_p}^{2/3} \quad (14)$$

Both correlations are valid in the inertial flow regime, and the particle diameter-based Reynolds number is defined as,

$$Re_{D_p} = \frac{U_f D_p}{\nu_a (1 - \varepsilon)} \quad (15)$$

3.2.2. Pressure drop

The air-side pressure drop was calculated by,

$$\Delta p = \frac{(1 - \varepsilon^2 + K_c)}{\varepsilon^2} \frac{\rho_{a,in}}{2} U_f^2 + \sum_1^{N_{CV}} f \frac{L_{CV}}{D_p} \rho_a U_f^2 \frac{(1 - \varepsilon)}{\varepsilon^3} - \frac{(1 - \varepsilon^2 - K_e)}{\varepsilon^2} \frac{\rho_{a,out}}{2} U_f^2 \quad (16)$$

where the first and third terms are the entrance and exit pressure losses, respectively. The contraction and expansion coefficients, K_c and K_e , were obtained from Shah and Sekulic [1], assuming a multiple-tube flat-tube core. The second term, which accounts for the frictional pressure drop (skin friction and form drag) in the porous matrix, derives from the Kozeny–Carman model for flow in porous media and incorporates the equivalent particle diameter defined above. In this study, the classical correlation due to Ergun [16],

$$f = \frac{150}{Re_{D_p}} + 1.75 \quad (17)$$

and the more recent correlation proposed by Montillet et al. [17],

$$f = 0.05 \left(\frac{D}{D_p} \right)^{0.20} \left[\frac{1000}{Re_{D_p} (1 - \varepsilon)} + \frac{60}{\sqrt{Re_{D_p} (1 - \varepsilon)}} + 12 \right] \quad (18)$$

were evaluated. In Eq. (17), D is the channel equivalent diameter.

3.2.3. Solution procedure

The mathematical model was implemented on the EES platform [21]. The number of control volumes in the flow direction was set equal to the number of tube rows. The input parameters of the model were the geometric characteristics of the heat exchanger (including the fin arrangements), the air and water flow rates and the inlet temperatures of both streams. For each control volume, Eq. (7) was solved iteratively for the outlet air temperature in the control volume, together with the energy balance for the water-side. The frictional pressure drop and the heat transfer rate were also calculated at each control volume. When the outlet section of the heat exchanger was reached, the total heat transfer rate was determined by summing up the heat transfer rates for each control volume. The total pressure drop was calculated by Eq. (16), and the average air-side thermal conductance was computed via Eq. (1) using the calculated outlet air and water temperatures and the total heat transfer rate.

4. Results

4.1. Experimental results

The experimental air-side thermal conductance as a function of the air flow rate is presented in Fig. 7. Due to the fact that the surface area did not vary significantly between the heat exchangers, for a given flow rate, the samples with the largest values of face area (D and E) exhibited the smallest values of thermal conductance as a result of the small face velocity experienced by these heat exchangers. This, as expected, led to low values of the local heat transfer coefficient. Sample C, whose surface area was the one but smallest, showed a higher thermal conductance than Samples A and D. This behavior can be explained in part by the comparatively high overall surface efficiency sustained by Sample C, which had a larger number of the smallest fin arrangements (R_1).

Mean values of the overall surface efficiency for each heat exchanger, defined as the arithmetic average of the overall surface efficiency of the control volumes Eq. (9), are shown in Table 2. The minimum and maximum values of the mean surface efficiency reported in the table are those obtained with the maximum and

Table 2

Minimum, average and maximum values of the mean overall surface efficiency calculated according to the heat exchanger model.

Sample	Minimum	Average	Maximum
A	0.876	0.912	0.955
B	0.935	0.958	0.987
C	0.945	0.964	0.987
D	0.960	0.978	0.993
E	0.984	0.991	0.999

minimum air flow rates, respectively, and give an idea of the sensitivity of the surface efficiency with respect to the air flow rate. The overall surface efficiency can also explain the difference between the values of the air-side thermal conductance of Samples A and B, which had the same geometric configuration but differed only in the value of fin thickness. In addition to having lower values of surface efficiency, the smaller thickness of the fins in Sample A also contributed to increasing the heat exchanger porosity, which gave rise to lower superficial air velocities. The difference between Samples D and E was caused by the difference between the surface area, which was large enough so that the air-side conductance of Sample D was higher than that of Sample E, despite the smaller porosity and larger surface efficiency of the latter.

A combined evaluation of the heat transfer and pumping power performances was carried out by means of the core volume goodness factors [1]. Fig. 8 shows the thermal conductance per unit volume, $\eta_o \bar{h}_o \beta$, as a function of the pumping power per unit volume, $\frac{\Delta p_a V_a}{A_o} \beta$. As expected, due to the highest superficial air velocities encountered in the heat exchangers with the smaller values of face area, Samples A, B and C exhibited the largest values of pumping power per unit volume for a given air-side heat transfer conductance. Among them, Sample A had the largest value of pumping power per unit volume chiefly because the thinner fins gave rise to the smallest overall surface efficiency, as can be seen from Table 2. Also, because of the largest porosity of Sample A, the *in-situ* velocities were lower and the heat transfer coefficient was slightly smaller than those of Samples B and C. Overall, the best performance was displayed by Sample E, which was also associated with

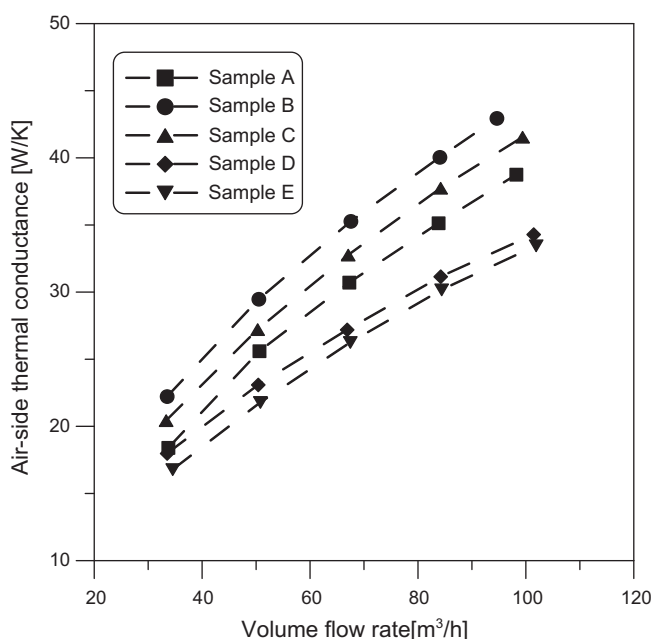


Fig. 7. Air-side thermal conductance as a function of the air flow rate.

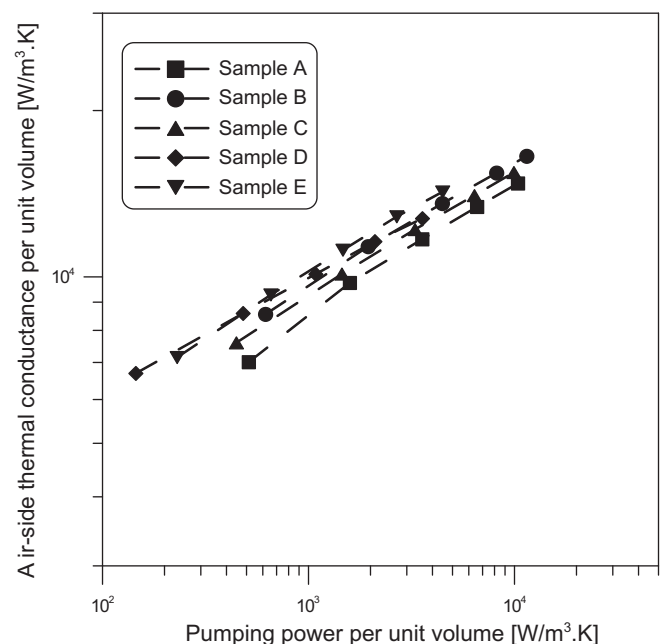


Fig. 8. Air-side thermal conductance per unit volume as a function of the pumping power per unit volume.

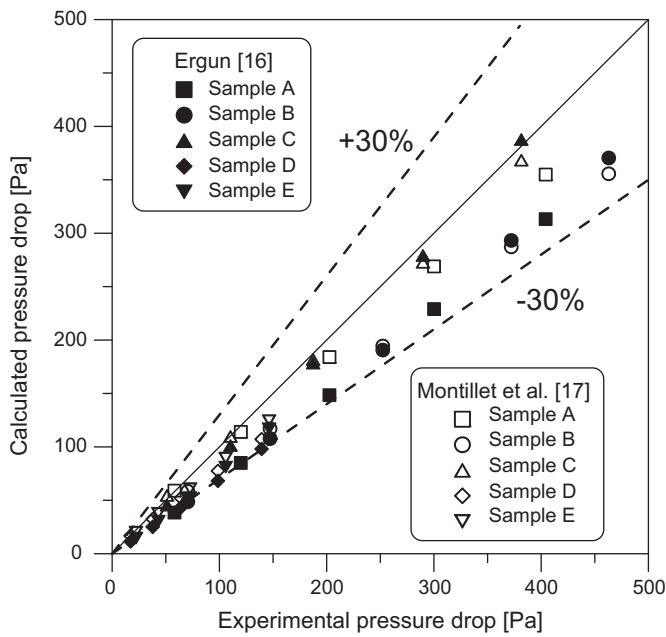


Fig. 9. Comparison of modeling and experimental results for the air-side pressure drop.

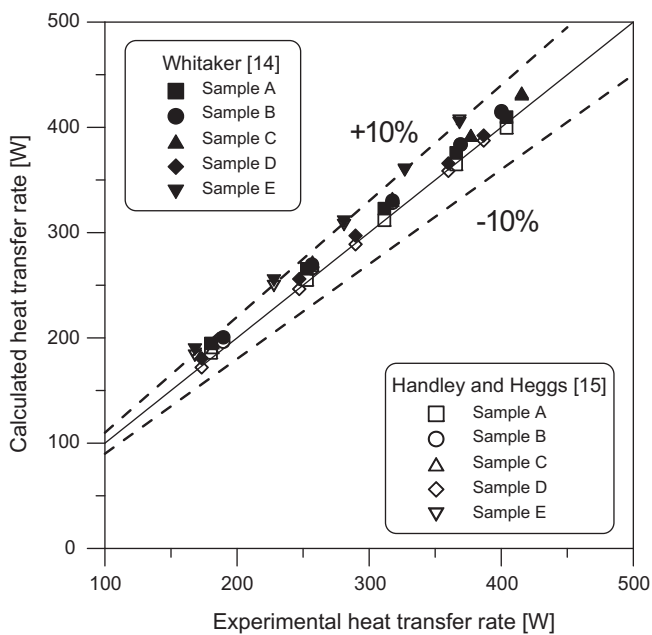


Fig. 10. Comparison of modeling and experimental results for the heat transfer rate.

its high surface efficiency and surface area density (compactness). This seemed to be enough to compensate for its slightly larger pressure drop in comparison to Sample D, which experienced a decrease in performance, relative to Sample E, as the flow rate increases.

4.2. Modeling results

Figs. 9 and 10 show a comparison of the pressure drop and heat transfer rate model predictions with the experimental data. The general agreement with the data was within the experimental uncertainty for the heat transfer rate but, as can be seen in Fig. 9,

there is a clear tendency for the friction factor correlations to underestimate the pressure drop. However, given the fact that the Ergun [16] and Montillet et al. [17] correlations were generated for low-porosity beds, with different kinds of porous structures (packed beds of spheres), the agreement can be considered satisfactory. On the other hand, for the heat transfer rate, both correlations predicted all data points to within ±10% error, with a slight tendency to overestimate the data. The prediction ability of the correlations can be compared based on the following statistical quantities,

$$RMS = \frac{100}{n} \sqrt{\sum_{i=1}^n \frac{(\xi_{cal,i} - \xi_{exp,i})^2}{\xi_{exp,i}^2}} \quad (19)$$

$$AAD = \frac{100}{n} \sum_{i=1}^n \left| \frac{\xi_{cal,i} - \xi_{exp,i}}{\xi_{exp,i}} \right| \quad (20)$$

$$Bias = \frac{100}{n} \sum_{i=1}^n \frac{\xi_{cal,i} - \xi_{exp,i}}{\xi_{exp,i}} \quad (21)$$

where ξ is a general variable (e.g. heat transfer rate or pressure drop). The results are summarized in Table 3. The Montillet et al. [17] and Handley and Heggs [15] correlations showed the best performances for the pressure drop and heat transfer rate predictions, respectively. Nevertheless, given the small differences between the values of RMS and AAD for the Handley and Heggs [15] and Whitaker [14] correlations, both methods can be applied without an appreciable loss of accuracy.

The behavior of the friction factor as a function of the Reynolds number is shown in Fig. 11. While the data trend was well picked-up by the Montillet et al. [17] correlation for a representative porosity of 0.825, the observed scatter suggested that the structure and the configuration of the fin arrangements in the porous matrix may be as important as the global parameters (e.g., porosity and particle diameter) in establishing the friction factor behavior. This became clear as the friction factor data for Samples A, B and D (which have identical fin units) followed virtually the same trend line, while the data for Samples C and E were associated with lower values of the friction factor. The size and orientation of the fin arrangements were responsible for producing zones of flow separation and recirculation in the heat exchanger matrix which were, due to the small values of fluid velocity associated with them, related to poor heat transfer from the solid surface. On the other hand, flow separation and recirculation are responsible for generating form drag, which increases the pressure drop. Thus, when the fin arrangement size or distribution is altered, one should expect the impact on the friction factor to be much more significant than that on the Nusselt number or Colburn j -factor. Indeed, this was exactly what Fig. 12 shows by plotting the calculated and experimental Nusselt numbers. In this case, both correlations showed a somewhat better agreement with the data, which seemed to depend much more on the value of the Reynolds number than on the fin structure/arrangement.

Table 3

Statistical quantities associated with the Nusselt number and friction factor correlations.

Correlation	RMS [%]	AAD [%]	Bias [%]
<i>Heat transfer rate</i>			
Whitaker [14]	1.3	5.5	5.5
Handley and Heggs [15]	1.0	3.8	3.6
<i>Pressure drop</i>			
Ergun [16]	5.0	23.1	-22.9
Montillet et al. [17]	2.9	12.3	-11.6

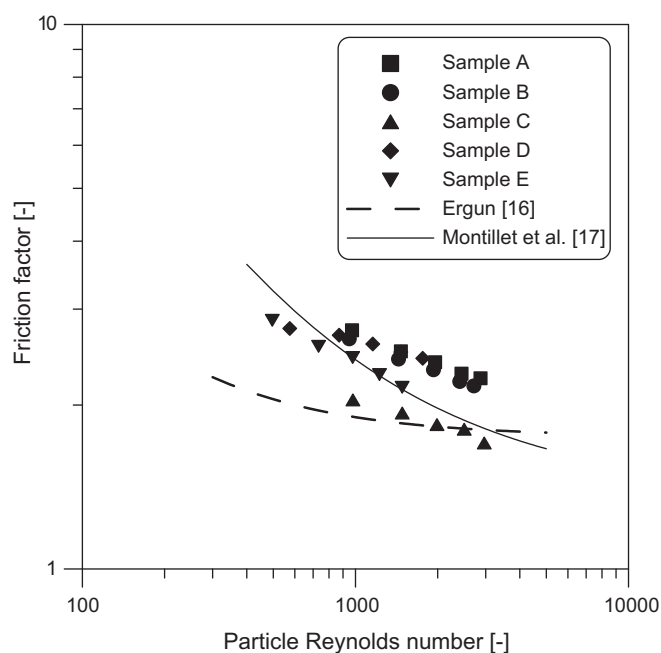


Fig. 11. Friction factor as a function of the Reynolds number. In the Montillet et al. [17] correlation, an average porosity of 0.825 was assumed.

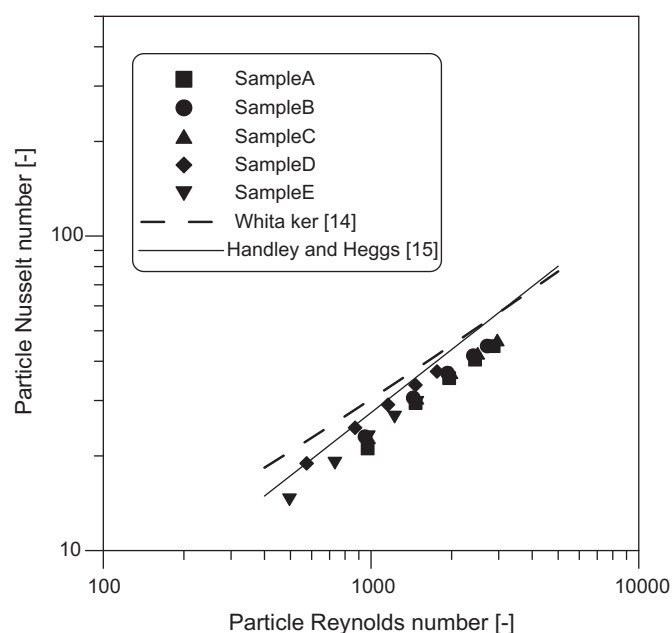


Fig. 12. Nusselt number as a function of the Reynolds number. In the Handley and Heggs [15] correlation, an average porosity of 0.825 was assumed.

5. Conclusions

A thermal-hydraulic evaluation of the peripheral fin heat exchanger was presented in this paper. The one-dimensional heat transfer analysis at the fin arrangement level [12] was incorporated into an overall heat exchanger calculation in order to predict the heat transfer rate and the air-side pressure drop. The heat exchanger model was based on the theory of porous media and incorporated the actual fin geometry and the fin temperature profiles into the calculation of the air-side porosity and of the overall surface efficiency, respectively. The model results were compared with those obtained in an open-loop wind tunnel calorimeter.

The best overall performance in terms of core volume goodness factors was achieved with a heat exchanger prototype (Sample E) with a large face area (and hence a smaller number of tube rows) and a large number of small fin arrangements, so that its overall surface efficiency was high compared to the other prototypes.

The model predicted the pressure drop and heat transfer rate data with an acceptable level of agreement. The best performances were achieved by the Montillet et al. [17] and Handley and Heggs [15] correlations, which showed RMS errors of 3% for the air-side pressure drop and 1% for the heat transfer rate, respectively. The Whitaker [14] correlation performed as well as the Handley and Heggs [15] method.

Acknowledgements

The material presented in this paper is a result of a long-standing technical-scientific partnership between UFSC and Embraco. Financial support from FINEP and CNPq through Grant No. 573581/2008-8 (National Institute of Science and Technology in Cooling and Thermophysics) is duly acknowledged.

References

- [1] R.K. Shah, D. Sekulic, *Fundamentals of Heat Exchanger Design*, Wiley, New York, 2003.
- [2] R.L. Webb, N-H. Kim, *Principles of Enhanced Heat Transfer*, second ed., Taylor and Francis, New York, 2005.
- [3] C-C. Wang, Technology review – A survey of recent patents of fin-and-tube heat exchangers, *J. Enhanced Heat Transfer* 7 (2000) 333–345.
- [4] C-C. Wang, A survey of recent patents on fin-and-tube heat exchangers from 2001 to 2009, *Int. J. Air Conditioning Refrigerat.* 18 (2010) 1–13.
- [5] A.M. Jacobi, Y. Park, D. Tafti, X. Zhang, An assessment of the state of the art, and potential design improvements, for flat-tube heat exchangers in air conditioning and refrigeration applications – Phase I, Final, Report, ARTI-21CR/20020-01, 2001.
- [6] J. Yin, A.M. Jacobi, Condensate retention effects on the air-side heat transfer performance of plain and wavy-louvered heat exchangers, ACRC Report No. TR-158, University of Illinois at Urbana-Champaign, IL, 2000.
- [7] A. D. Tang, A. M. Jacobi, Air-side heat transfer with highly interrupted surfaces: An experimental study of condensate retention effects, ACRC Report No. TR-185, University of Illinois at Urbana-Champaign, IL, 2001.
- [8] J. Kim, M. Kaviany, Purging of dropwise condensate by electrowetting, *J. Appl. Phys.* 101 (2007). 103520-1-7.
- [9] J. Kim, M. Kaviany, Electrowetting purged surface condensate in evaporators, *Heat Transfer Eng.* 31 (2010) 101–107.
- [10] F. T. Knabben, C. J. L. Hermes, C. Melo, Numerical assessment of frosting and defrosting of 'no-frost' evaporators, in: J.E. Braun (Ed.), *Proceedings of the Thirteenth International Refrigeration and Air Conditioning Conference at Purdue*, West Lafayette, IN, 2010, paper 2111.
- [11] F. T. Knabben, C. J. L. Hermes, C. Melo, An in-situ study of frost accretion on no-frost evaporators, in: F. Gori (Ed.), *Proceedings of the ASME-ATI-UIT Conference on Thermal and Environmental Issues in Energy Systems*, Sorrento, Italy, 2010, pp. 505–510.
- [12] H. Wu, D. Ma, M. Kaviany, Peripheral fins for blockage robustness, *Int. J. Heat Mass Transfer* 50 (2007) 2514–2520.
- [13] B. F. Pussoli, J. R. Barbosa Jr., L. W. da Silva, M. Kaviany, Air-side heat transfer and pressure drop characteristics of peripheral fin heat exchangers, in: A. Bar-Cohen (Ed.), *Proceedings of the Fourteenth International Heat Transfer Conference IHTC14*, Washington, DC, 2010, paper IHTC14-23037.
- [14] S. Whitaker, Forced convection heat transfer correlations for flow in pipes, past flat plates, single cylinders, single spheres, and for flow in packed beds and tube bundles, *AIChE J.* 18 (1972) 361–371.
- [15] D. Handley, P. J. Heggs, Momentum and heat transfer mechanisms in regular shaped packings, *Transactions of the Institution of Chemical Engineers* 46 (1968) paper T251.
- [16] S.S. Ergun, Fluid flow through packed columns, *Chem. Eng. Prog.* 48 (1952) 89–94.
- [17] A. Montillet, E. Akkari, J. Comiti, About a correlating equation for predicting pressure drops through packed beds of spheres in a large range of Reynolds numbers, *Chem. Eng. Process.* 46 (2007) 329–333.
- [18] P.J. Waltrich, J.R. Barbosa Jr., C.J.L. Hermes, C. Melo, Air-side heat transfer and pressure drop characteristics of accelerated flow evaporators, *Int. J. Refrigerat.* 34 (2011) 484–497.
- [19] ANSI/ASHRAE 51, Laboratory methods of testing fans for aerodynamic performance rating, Atlanta, GA, 1999.
- [20] B.F. Pussoli, Analysis and optimization of peripheral finned-tube evaporators, M.Eng. Dissertation, Federal University of Santa Catarina, 2010.
- [21] S.A. Klein, Engineering equation solver, Professional version V8.528, 2010.
- [22] M. Kaviany, *Essentials of Heat Transfer*, Cambridge University Press, New York, 2011.